Chinese Chemical Letters 36 (2025) 109800

Contents lists available at ScienceDirect

Chinese Chemical Letters

journal homepage: www.elsevier.com/locate/cclet

The effect of electron-phonon coupling on the photoluminescence properties of zinc-based halides

Zheyu Li[a,b], Huwei Li[a], Yao Li[a,b], Xinyu Fu[a,b], Hongxia Yue[a,b], Qingxing Yang[a,b], Jing Feng[a,b,*], Xinyu Wang[a,*], Hongjie Zhang[a,b,c,*]

[a] State Key Laboratory of Rare Earth Resource Utilization, Changchun Institute of Applied Chemistry, Chinese Academy of Sciences, Changchun 130022, China
[b] School of Applied Chemistry and Engineering, University of Science and Technology of China, Hefei 230026, China
[c] Department of Chemistry, Tsinghua University, Beijing 100084, China

ARTICLE INFO

Article history:
Received 27 November 2023
Revised 29 February 2024
Accepted 20 March 2024
Available online 20 March 2024

Keywords:
Metal halides
Electron-phonon coupling
Huang-Rhys factor
Self-trapping excitons
ns^2 electrons

ABSTRACT

Self-trapping excitons (STEs) emission in metal halides has been a matter of interest, correlating with the strength of electron-phonon coupling in the lattice, which are usually caused by ions with ns^2 electronic structure. In this work, Sb^{3+}/Te^{4+} ions doped Zn-based halide single crystals (SCs) with two STEs emissions have been synthesized and the possibility of its anti-counterfeiting application was explored. Further, the relationship between the strength of electron-phonon coupling and photoluminescence quantum yields (PLQYs) for STEs in a series of metal halides has been studied. And the semi-empirical range of the Huang-Rhys factors (*S*) for metal halides with excellent photoluminescence (PL) property has been summarized. This work provides ideas for further research into the relationship between luminescence performance and electron-phonon coupling of metal halides, and also provides a reference for designing the metal halides with high PLQYs.

Lead-based halide materials as a new generation of optoelectronic materials have attracted much attention in light emitting diodes (LEDs) [1–4], photodetectors [5–9], scintillators [10–14], and solar cells [15–19], due to their direct and adjustable bandgap, strong light absorption coefficient, and high photoluminescence quantum yield (PLQY). However, due to the physical and chemical instability and the toxicity of Pb^{2+}, there are certain limitations in their applications, therefore, the study of lead-free halide materials has attracted much attention. A series of metal ions have been served to replace lead ions to avoid the drawbacks of lead-based halide materials. A possible non-toxic alternative is substitution of Pb^{2+} with the similar electronic configurations such as Sn^{2+}, Ge^{2+} [20,21]. However, the main issue with Sn^{2+} or Ge^{2+} is that they are easily oxidized to tetravalence, thereby damaging the crystal structure and photoelectric properties of halide materials [22]. Zinc ions, as divalent ions, have the potential to replace lead ions due to their non-toxicity and stable valence [23].

Self-trapped excitons (STEs) emission have gained much attention owing to large Stokes shift and broadband emission characteristics in metal halide materials [24–26]. In the soft lattice, when the electron-phonon interaction is strong enough, the electron-hole pairs of the excited state will cause elastic distortion in the lattice around them, thus forming the self-trapping. The Huang-Rhys factor (*S*), as a dimensionless constant, is usually used to describe the coupling strength of electrons and phonons in the lattice. It has been confirmed that the higher *S* value, the stronger electron-phonon coupling strength, and the greater possibility of STEs formation [27]. Excessive *S* can bring broadband emissions, but it will also cause the excitons in the excited state to emit phonons through non-radiative recombination and return to the ground state [28]. In other words, in order to achieve efficient emission of STEs, *S* should be an appropriate value, neither too large nor too small. However, the appropriate range of values for *S* has not been summarized.

Ion doping is an important method to improve the luminescent performance of lead-free halide materials [29]. Ions with typical ns^2 electronic structure such as Sb^{3+}, Te^{4+}, Bi^{3+} are usually served as dopants to regulate the luminescence of halide materials because they can induce STEs emission in lead-free halide materials [30–35]. Due to electron-interaction and spin-orbit coupling matrix, nsnp excited configuration in ns^2 ions would split into four energy states $^3P_0$, $^3P_1$, $^3P_2$, and $^1P_1$. Generally, the transitions $^1S_0 \rightarrow {}^3P_0$ and $^1S_0 \rightarrow {}^3P_2$ are forbidden. However, $^1S_0 \rightarrow {}^3P_1$ and $^1S_0 \rightarrow {}^1P_1$ transitions are parity-allowed because of the spin–orbit

* Corresponding authors.
E-mail addresses: fengj@ciac.ac.cn (J. Feng), wangxysir@ciac.ac.cn (X. Wang), hongjie@ciac.ac.cn (H. Zhang).

https://doi.org/10.1016/j.cclet.2024.109800
1001-8417/

coupling [25]. Therefore, doping ions with ns^2 outermost electronic configuration can provide new absorption and emission centers. Moreover, ns^2 electrons doped halide materials with broadband emission and large Stokes shift, which can effectively avoid self-absorption, are highly desirable for optical applications. Although single exciton emission has the characteristics of large Stokes shift and broadband emission, it still has some limitations, thus multiple exciton emissions have been considered. The multiple exciton emissions in single material have fundamental and practical implications in imaging, lighting applications and optoelectronic research [36,37]. For instance, the production of lighting devices such as white LEDs require multiple exciton emissions to boost color rendering performance. Consequently, it is necessary to dope a variety of ns^2 ions into lead-free halide materials to produce multiple exciton emissions and to study the excitation-acoustic coupling of various STEs.

Herein, Cs_2ZnCl_4 SCs doped with Sb^{3+} and Te^{4+} have been fabricated by hydrothermal synthesis method. Taking advantage of the fact that ions with ns^2 electron structure can produce STEs emission, a series of anti-counterfeiting patterns have been prepared to achieve information encryption base on the varied luminescence characteristics of Cs_2ZnCl_4:Sb^{3+},Te^{4+} SCs excited by selective excitation wavelengths. By analyzing the PL properties of the prepared zinc-based halides, we further studied the relationship between electron-phonon coupling of STEs and PLQYs, and summarized the semi-empirical range (25–40) of Huang-Rhys factors (*S*) for metal halides with excellent PL property based on the collected references.

Sb^{3+} and Te^{4+} co-doped Cs_2ZnCl_4 SCs were synthesized through a hydrothermal synthesis method using $ZnCl_2$, $SbCl_3$, $TeCl_4$, CsCl, and concentrated HCl as the ingredients. Cs_2ZnCl_4:x%Sb^{3+},y%Te^{4+} means the feeding ratios of Sb/Zn and Te/Zn are x% and y%, respectively. The detailed synthesis procedure is provided in experimental section. Cs_2ZnCl_4 SCs crystallize in orthorhombic space group *Pnma* [38]. According to Fig. 1a, Cs_2ZnCl_4 belongs to typical zero-dimensional (0D) structure that Zn^{2+} ions occupy the center position of $[ZnCl_4]^{2-}$ tetrahedrons and the isolated $[ZnCl_4]^{2-}$ tetrahedrons are completely separated by peripheral Cs^+ cations. According to powder X-ray diffraction (PXRD) patterns, Cs_2ZnCl_4 SCs with different doping concentrations of Sb^{3+} and Te^{4+} ions match well with the standard pattern of Cs_2ZnCl_4 (ICSD card No. 10-0318) (Fig. 1b). As shown in Fig. 1c, Cs_2ZnCl_4:Sb^{3+},Te^{4+} SCs present transparent under the natural light and become red exposed to 302 nm UV light, then turn yellow under the 395 nm light irradiation. And the corresponding PL spectra and CIE chromaticity are shown in Fig. S1 (Supporting information). Sb^{3+} and Te^{4+} ions were found to be uniformly distributed in Cs_2ZnCl_4 SCs according to energy dispersive X-ray spectroscopy (EDS) mapping (Fig. 1d). X-ray photoelectron spectroscopy (XPS) reveals the valence states of Sb^{3+}, Te^{4+} and Zn^{2+} in Cs_2ZnCl_4:Sb^{3+},Te^{4+} SCs (Fig. 1e, Figs. S2a and b in Supporting information). Inductively coupled plasma optical emission spectrometry (ICP-OES) (Tables S1 and S2 in Supporting information) revealed that the actual Te^{4+} and Sb^{3+} concentrations are lower than its feeding concentrations, because the valence states of Te^{4+} and Sb^{3+} ions are different from Zn^{2+}.

According to Fig. S2c (Supporting information), ultraviolet–visible (UV–vis) absorption spectra revealed that Sb^{3+} and Te^{4+} doping could introduce additional absorption peaks in the 250–500 nm range. Figs. 2a and b show that photoluminescence excitation (PLE) and photoluminescence (PL) spectra of Cs_2ZnCl_4:30%Sb^{3+} SCs and Cs_2ZnCl_4:5%Te^{4+} SCs, suggesting that they both feature broadband emissions and large Stokes shift. It could be seen that the broad red emission of Cs_2ZnCl_4:Sb^{3+} SCs centered at 720 nm with full-width at half-maximum (FWHM) of 190 nm comes from STEs emission of Sb^{3+} and the yellow emission of Cs_2ZnCl_4:Te^{4+} SCs centered at 590 nm (FWHM of 119 nm) originates from STEs emission of Te^{4+}. The PLE spectrum of Cs_2ZnCl_4:30%Sb^{3+} contains two peaks at 260 and 315 nm, the former corresponds to the excitation peak of Cs_2ZnCl_4 matrix and the latter results from the contribution of Sb^{3+} orbitals [39]. The PLE and PL spectra of pure Cs_2ZnCl_4 are given in Fig. S3 (Supporting information), and it is indicated that Sb^{3+} and Te^{4+} ions successfully enter Cs_2ZnCl_4 unit cells and replace Zn^{2+} ions to occupy the center of the tetrahedrons [39,40]. Temperature-dependent PL spectra of Cs_2ZnCl_4:30%Sb^{3+} and Cs_2ZnCl_4:5%Te^{4+} SCs are measured from 100 K to 270 K (Figs. 2c and d). The PL intensity of Cs_2ZnCl_4:30%Sb^{3+} decreased gradually with increasing temperature, together with the blueshift of the PL peak, owing to the stronger nonradiative relaxation and electron-phonon coupling of Sb^{3+} when the temperature become higher [41]. The emission intensity of Te^{4+} decreased as the temperature increasing, which is associated with vibrational relaxation. To reveal the influence of electron-phonon coupling and obtain the Huang-Rhys factor (*S*), we

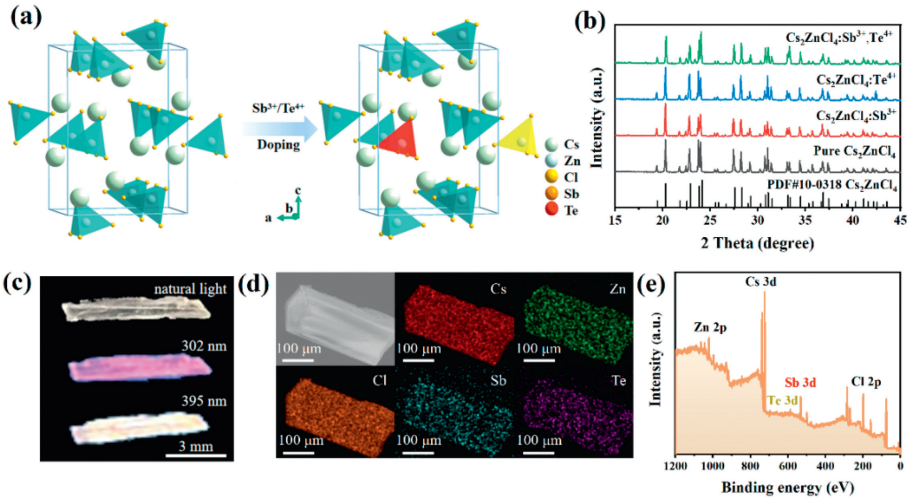

Fig. 1. Structural and compositional characterization of Cs_2ZnCl_4:Sb^{3+},Te^{4+} SCs. (a) Crystal structure diagram of Cs_2ZnCl_4. (b) Comparison of PXRD patterns of Cs_2ZnCl_4 doped with different contents of Te^{4+} and Sb^{3+}. (c) Optical microscopic images of Cs_2ZnCl_4:Sb^{3+},Te^{4+} SCs under natural light (top), 302 nm UV light (middle), and 395 nm UV light (bottom). (d) EDS mappings of Cs_2ZnCl_4:Sb^{3+},Te^{4+} SCs. (e) XPS spectrum of Cs_2ZnCl_4:Sb^{3+},Te^{4+}.

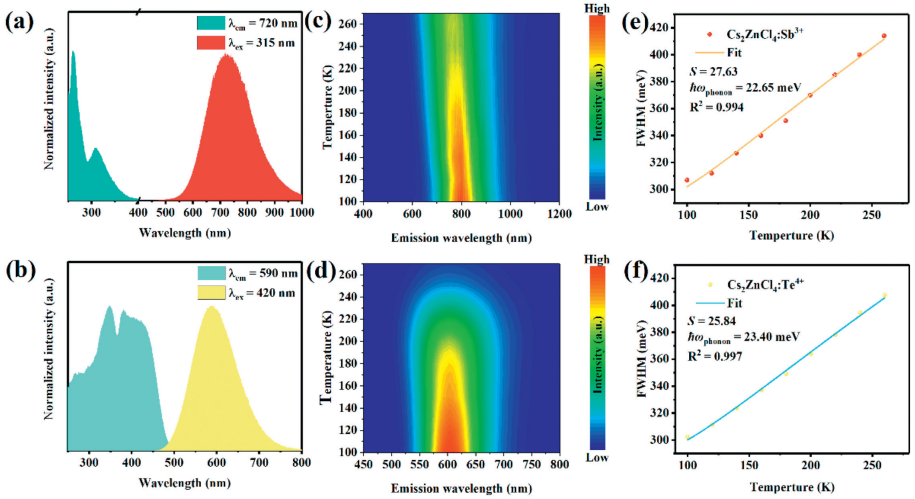

Fig. 2. Normalized PL and PLE spectra of as-prepared (a) Cs_2ZnCl_4:30%Sb^{3+} SCs and (b) Cs_2ZnCl_4:5%Te^{4+} SCs. Pseudo color mapping of temperature-dependent PL spectra of (c) Cs_2ZnCl_4:30%Sb^{3+} SCs upon excitation at 315 nm and (d) Cs_2ZnCl_4:5%Te^{4+} SCs upon excitation at 420 nm along with temperature range from 100 K to 270 K. FWHM of the PL spectra as a function of temperature for (e) Cs_2ZnCl_4:30%Sb^{3+} SCs and (f) Cs_2ZnCl_4:5%Te^{4+} SCs, data are fitted by Eq. 1.

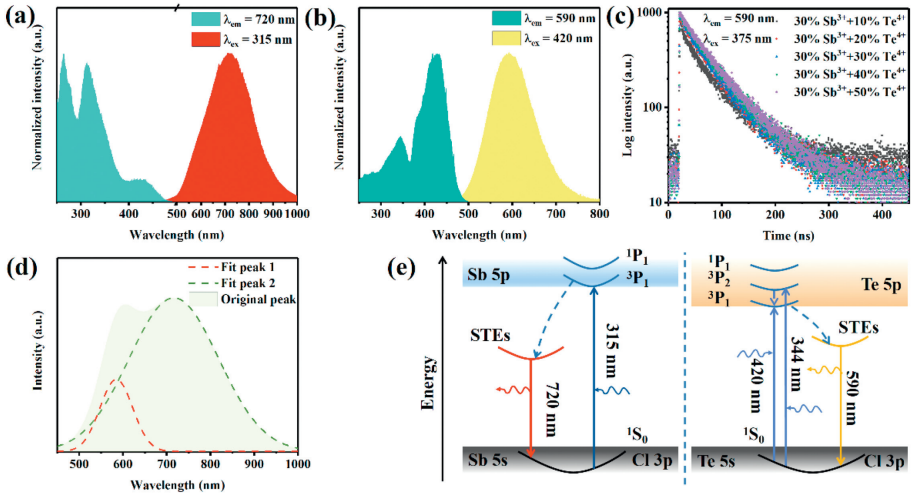

Fig. 3. Optical characterization of Cs_2ZnCl_4:30%Sb^{3+},40%Te^{4+} SCs. (a) PLE (λ_{em} = 720 nm) and PL (λ_{ex} = 315 nm) spectra of Cs_2ZnCl_4:30%Sb^{3+},40%Te^{4+} SCs. (b) PLE (λ_{em} = 590 nm) and PL (λ_{ex} = 420 nm) spectra of Cs_2ZnCl_4:30%Sb^{3+},40%Te^{4+} SCs. (c) Decay curves of Cs_2ZnCl_4:Sb^{3+},Te^{4+} SCs with different Te^{4+} doping concentrations. (d) PL spectrum and fitting curves of Cs_2ZnCl_4:30%Sb^{3+},40%Te^{4+} SCs under 365 nm excitation. (e) Energy level diagram of Cs_2ZnCl_4:30%Sb^{3+},40%Te^{4+} SCs showing the excitation and emission processes.

analyzed the FWHM according to Eq. 1:

$$\mathrm{FWHM} = 2.36\sqrt{S}\hbar\omega_{\mathrm{phonon}}\sqrt{\coth\left(\left(\hbar\omega_{\mathrm{phonon}}\right)/\left(2k_BT\right)\right)} \quad (1)$$

where the $\hbar\omega_{phonon}$ is the phonon energy, k_B is the Boltzmann constant. The Huang-Rhys factor (S) and the phonon energy ($\hbar\omega_{phonon}$) are 27.63 and 22.65 meV for Cs_2ZnCl_4:30%Sb^{3+}, respectively (Fig. 2e). For Cs_2ZnCl_4:5%Te^{4+} SCs, S is 25.84 and $\hbar\omega_{phonon}$ is 23.40 meV (Fig. 2f). Such large S values indicate the strong electron-phonon coupling of Te^{4+} and Sb^{3+} in Cs_2ZnCl_4, which is responsible for the broadband and large Stokes shift of Sb^{3+} (445 meV, 405 nm) and Te^{4+} (420 meV, 170 nm) emissions.

Based on the wide emission characteristics of STEs from Te^{4+} and Sb^{3+}, we further synthesized Cs_2ZnCl_4:Sb^{3+},Te^{4+} SCs. Compared with Cs_2ZnCl_4:Sb^{3+} and Cs_2ZnCl_4:Te^{4+} SCs, PL of Cs_2ZnCl_4:Sb^{3+},Te^{4+} SCs are almost the same, however, PLE of Cs_2ZnCl_4:Sb^{3+},Te^{4+} SCs come from the superposition of PLE of Cs_2ZnCl_4:Sb^{3+} and Cs_2ZnCl_4:Te^{4+} SCs (Figs. 3a and b). Firstly, we synthesized Sb^{3+} doped Cs_2ZnCl_4 SCs with Sb/Zn feeding ratio of 10%, 20%, 30%, 40% and 50% (Fig. S4 in Supporting information). The actual Sb^{3+} doping concentrations are shown in Table S1 (Supporting information). It could be seen that with increasing Sb^{3+} doping concentration, the emission of Cs_2ZnCl_4:Sb^{3+} first increases and then decreases owing to the concentration quenching effect, achieving a maximum of FWHM up to 192 nm when the feeding ratio of Sb/Zn is 30% (Fig. S5a in Supporting information). According to the PL decay curves of Cs_2ZnCl_4:Sb^{3+} SCs, the lifetime based on single exponential-fitting is calculated to be 12.61, 12.68, 13.07, 12.84 and 12.10 μs for Cs_2ZnCl_4:10%−50%Sb^{3+}, respectively (Fig. S5b in Supporting information). In addition, the lifetimes of Cs_2ZnCl_4:Sb^{3+} SCs show firstly a slightly monotonic increase and then decrease with increasing Sb^{3+} concentration. This is related to the increased non-radiative transition [42]. From the optimal concentration of Sb^{3+} doping, we further doped Te^{4+} with different concentrations from 10% to 50% to form Cs_2ZnCl_4:Sb^{3+},Te^{4+} SCs. From the PL spectra of Cs_2ZnCl_4:Sb^{3+},Te^{4+} SCs (Fig. S6a in Supporting information), it was found that the emission intensity also increases and then decreases with increasing the feeding ratio, satisfying the concentration quenching effect, and the optimum doping concentration of Te^{4+} was determined to be 40%.

Time-resolved photoluminescence decay experiments (Fig. 3c) show that the lifetimes measured at 590 nm are 47.48, 52.49, 52.53, 58.41 and 56.80 ns for 10%–50%Te^{4+} co-doped Cs_2ZnCl_4 SCs, respectively, which are comparable to the decay lifetimes of STEs emissions of reported low-dimensional metal halides [40,43]. It can be easily seen from Fig. 3c that under 375 nm excitation, the decay times of the inherent radiation for different Te^{4+} concentrations monitored at 590 nm also firstly increase and then decrease slightly with increasing Te^{4+} concentration, which is associated with the non-radiative transition [42]. Furthermore, the lifetimes of Cs_2ZnCl_4:30%Sb^{3+},y%Te^{4+} monitored at 720 nm have been collected in Fig. S6b (Supporting information) and there is almost no significant change with the change of Te^{4+} concentration. As a result, we believe that Cs_2ZnCl_4:30%Sb^{3+},40%Te^{4+} SCs are the appropriate choice for subsequent discussion of Sb^{3+} and Te^{4+} co-doped Cs_2ZnCl_4 SCs. From Fig. 3d, the PL emission band ($\lambda_{ex}=365$ nm) could be fitted as fit peaks 1 and 2, corresponding to Sb^{3+} and Te^{4+} emission, respectively, indicating the formation of double broad peaks of emission under the same excitation. Based on previous reports, the origins of PL of Cs_2ZnCl_4:Sb^{3+},Te^{4+} SCs are illustrated in Fig. 3e [44,45]. Upon different excitations, electrons are first excited from 5s states of Sb^{3+} or Te^{4+} ions to their 5p states and then trapped in $[SbCl_4]^-$ or $[TeCl_4]$ tetrahedrons, which sequentially induced triplet dopant STEs, respectively. For Te^{4+} ions, by considering the contribution of lattice vibration to the transition process and the transition selection law, the high-energy band of PLE could be attributed to the $^1S_0 \rightarrow {}^3P_2$ transition of Te^{4+} *via* spin–orbit coupling, which is a double peak due to the Jahn-Teller effect. And the low-energy band of PLE is attributed to the $^1S_0 \rightarrow {}^3P_1$ transition of Te^{4+} [46]. Besides, the PLQYs of Cs_2ZnCl_4:30%Sb^{3+} and Cs_2ZnCl_4:5%Te^{4+} are 15.2% and 1.3%, respectively (Fig. S7 in Supporting information), the PLQY of Cs_2ZnCl_4:30%Sb^{3+},40%Te^{4+} is 0.8% (Fig. S8a in Supporting information). According to Fig. 2 and Figs. S8b and c (Supporting information), S of Cs_2ZnCl_4:Sb^{3+}, Cs_2ZnCl_4:Te^{4+} and Cs_2ZnCl_4:30%Sb^{3+},40%Te^{4+} are determined to be 27.63, 25.84 and 17.13, respectively. It seems to be a correlation between PLQYs and S.

In metal halide materials, the electron-phonon interaction plays an important role in the optical and electrical properties. As a dimensionless parameter, the S is mainly used to describe the strength of electron-phonon interaction. Generally speaking, when $S >> 1$, the electron-phonon interaction is characterized as strong coupling. Conversely, when $S << 1$, the electron-phonon interaction is considered to be weak coupling. For the STEs formation, the excitons are subject to carrier-phonon interaction, relaxation processes and internal conversion, and lose the energy known as self-trapping energy (E_{st}). Owing to strong coupling between phonons and excitons leading to lattice distortion, STEs emissions are typically characterized by broadband emission with FWHM of more than 60 nm. The lattice distortion energy (E_d) and ground state energy (E_{GS}) increase as the energy of STEs decreases during lattice distortion. Therefore, the emission energy (E_{PL}) can be described with the equation $E_{PL}=E_g-E_b-E_{st}-E_d$, where E_g is bandgap energy and E_b is exciton binding energy. The well-known S-factor is used to assess the tendency of STEs formation. Both S and E_{st} describe the degree of stabilization of the self-trapped state with respect to the untrapped state, resulting in the Stokes shift. The coordinate difference (ΔQ) between STEs and free excitons (FEs) is directly proportionate to S, based on $\Delta Q=S^{1/2}$. According to this formula, it can be concluded that the larger S, the greater the Stokes shift of self-trapped exciton emission.

The Huang-Rhys factor (S) also affects PL emission *via* the Franck-Condon factor. And the Franck-Condon factor is calculated by the recurrence method [47]. Assuming that the excited and ground states have similar phonon frequencies, the Franck-Condon factor (F, at zero temperature) could be simplified as

$$F=\left|\left\langle \chi_n|\chi_m\right\rangle\right|^2=\exp(-S)S^n/n! \quad (2)$$

where χ_m is the excited state harmonic phonon wavefunctions and χ_n is the ground state harmonic phonon wavefunctions. The photoluminescence peak appears at $n\approx S$, thus

$$F_{max}=\exp(-S)S^n/S! \quad (3)$$

which is a monotonic decreasing function of S. Since the PL intensity is proportionate to S, the larger S, the smaller the radiative rate and the lower the emission efficiency. Therefore, the S could be potentially used as the key for the design of efficient STEs emission. To obtain effective emission of STEs, the Huang-Rhys factor should be intermediate. When the S is overly large, there is strong phonon assisted non-radiative recombination, however, the too small S can disrupt the stability of the STEs state and weaken broadband emission. The S and PLQYs of various metal halide materials are collected in Table S3 (Supporting information) to get more specific semi-empirical range of S. In order to be more intuitive, a scatter diagram with S as x axis and PLQY as y axis has been provided in Fig. S9 (Supporting information). When S of metal halide materials is below 25 or above 40, the PLQYs of halide materials we collected become lower. In other words, S of metal halide luminescent materials with excellent PLQY is between 25 and 40. The PLQY of Cs_2ZnCl_4:30%Sb^{3+} with S in such semi-empirical range increases by order of magnitude compared with that of Cs_2ZnCl_4:5%Te^{4+} and Cs_2ZnCl_4:30%Sb^{3+},40%Te^{4+}. The semi-empirical range of S might be used as a reference for finding materials with high PLQYs. It is worth noting that the extent of PLQY is not entirely dependent on S, it is also closely related to factors such as substrate material, type and concentration of doping ion, volume defects. The PLQY of the synthesized Cs_2ZnCl_4:30%Sb^{3+} is not high enough, possibly due to the volume defects produced during the rapid cooling process in the synthesis process, thus reducing the luminescence.

In addition to the ultra-wide emission of Sb^{3+} and Te^{4+} STEs, Cs_2ZnCl_4:30%Sb^{3+},40%Te^{4+} SCs also have excellent environmental stability. The thermogravimetric analysis (Fig. S10a in Supporting information) shows that Cs_2ZnCl_4:30%Sb^{3+},40%Te^{4+} SCs have exceptional thermal stability because it does not decompose until 600 °C, which is fully compatible with the use of the material under normal conditions. Moreover, as shown in the unchanged PXRD patterns after five months of exposure to the ambient atmosphere (Fig. S10b in Supporting information), Cs_2ZnCl_4:30%Sb^{3+},40%Te^{4+} SCs overcome the humidity sensitivity of lead halide materials. After five months, the luminescence intensity of the SCs remained at a high level, with 80.4% of the initial PL intensity for Te^{4+} and 89.5% for Sb^{3+} (Fig. S11 in Supporting information). The above results demonstrate the excellent stability of Cs_2ZnCl_4:Sb^{3+},Te^{4+} SCs, which gives them further potential for practical applications.

The multi-exciton emissions of Cs_2ZnCl_4:Sb^{3+},Te^{4+} SCs enable dynamic color emissions by precisely adjusting the excitation wavelength (Figs. 4a and b). For instance, 315 nm light mainly excites the STEs of Sb^{3+}, resulting in red emission, and 420 nm excitation light mostly excites the STEs of Te^{4+} to produce yellow emission (Fig. 4c). Since the excitation spectra of Sb^{3+} STEs and the Te^{4+} STEs partially intersect, Cs_2ZnCl_4:Sb^{3+},Te^{4+} SCs can achieve continuous adjustable emission from red to yellow by changing the excitation wavelength from 315 nm to 420 nm. The color coordinates of yellow emission at 590 nm is (0.5054, 0.4789) and the color coordinates of red emission at 716 nm is (0.5634, 0.4214). The excitation-dependent emission of Cs_2ZnCl_4:Sb^{3+},Te^{4+} SCs offers a possibility for the encryption of information. The encryption and decryption process are presented in Fig. 4d and a series of anti-counterfeiting patterns are produced by using the powder ground of Cs_2ZnCl_4:Sb^{3+},Te^{4+} SCs and Cs_2ZnCl_4:Sb^{3+} (Fig. 4e). As a proof-of-concept, Cs_2ZnCl_4:Sb^{3+},Te^{4+} and Cs_2ZnCl_4:Sb^{3+} powder

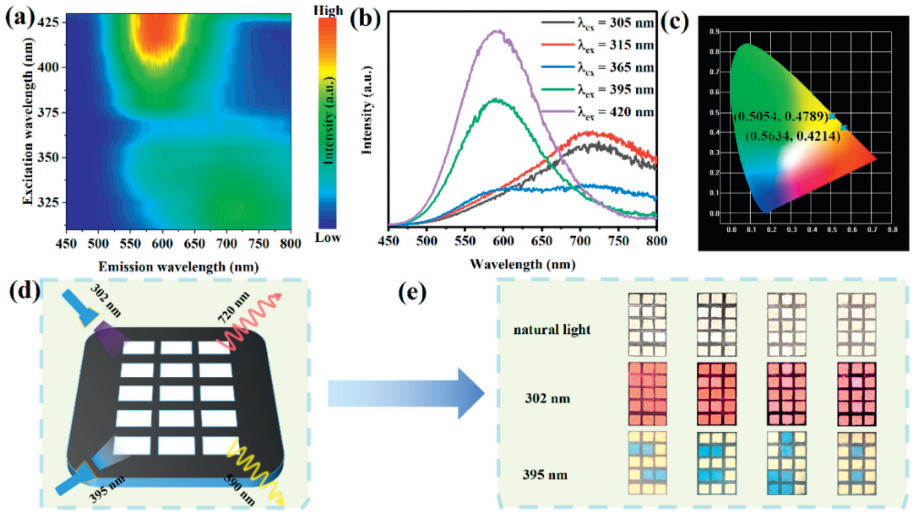

Fig. 4. Dynamic color delivery in $Cs_2ZnCl_4:Sb^{3+},Te^{4+}$ SCs. (a) Contour plot of excitation-dependent PL of Cs_2ZnCl_4:30%Sb^{3+},40%Te^{4+} SCs. (b) PL spectra of Cs_2ZnCl_4:30%Sb^{3+},40%Te^{4+} SCs under different excitation wavelengths. (c) The corresponding CIE chromaticity coordinates of Cs_2ZnCl_4:30%Sb^{3+},40%Te^{4+} SCs under 302 nm (bottom) and 395 nm (top) excitation. (d) Schematic diagram of information encryption. (e) Pattern encryption and decryption process under natural light (top), 302 nm UV light (middle) and 395 nm light (bottom).

were selectively filled to obtain different pixelated patterns (3×5 dot matrix). The pattern composed of $Cs_2ZnCl_4:Sb^{3+},Te^{4+}$ and $Cs_2ZnCl_4:Sb^{3+}$ powder appeared uniformly red under 302 nm excitation. However, under the excitation of 395 nm lamp, cryptographic information emerged as orange emission owing to chromatic luminescence switching of $Cs_2ZnCl_4:Sb^{3+},Te^{4+}$ SCs and displayed the numbers "2,3,4,8" separately. These performances indicate the SCs have great potential for anti-counterfeiting application.

In summary, we synthesized Zn-based halides doped with Sb^{3+} and Te^{4+}, and investigated the STEs emissions. Furthermore, we fabricated the anti-counterfeit patterns based on the continuously tunable emissions of $Cs_2ZnCl_4:Sb^{3+},Te^{4+}$ SCs to achieve the effect of information encryption. The relationship between electron-phonon coupling of STEs and PLQYs was studied. Based on the collected references, the semi-empirical range of the Huang-Rhys factors for metal halide materials with excellent PL property has been summarized, which could provide the reference for designing the high-performance metal halide materials.

Declaration of competing interest

The authors declare that they have no known competing financial interests or personal relationships that could have appeared to influence the work reported in this paper.

Acknowledgments

This work was supported by the financial aid from the National Natural Science Foundation of China (No. 22271273), and International Partnership Program of Chinese Academy of Sciences (No. 121522KYSB20190022).

Supplementary materials

Supplementary material associated with this article can be found, in the online version, at doi:10.1016/j.cclet.2024.109800.

References

[1] N. Wang, L. Cheng, R. Ge, et al., Nat. Photonics 10 (2016) 699–704.
[2] K. Lin, J. Xing, L.N. Quan, et al., Nature 562 (2018) 245–248.
[3] J. Song, J. Li, X. Li, et al., Adv. Sci. 27 (2015) 7162–7167.
[4] Y. Hong, C. Yu, H. Je, et al., Adv. Sci. 10 (2023) 2302906.
[5] J. Peng, C.Q. Xia, Y. Xu, et al., Nat. Commun. 12 (2021) 1531.
[6] L. Dou, Y. Yang, J. You, et al., Nat. Commun. 5 (2014) 5404.
[7] Y. Fang, Q. Dong, Y. Shao, Y. Yuan, J. Huang, Nat. Photonics 9 (2015) 679–686.
[8] H. Wei, Y. Fang, P. Mulligan, et al., Nat. Photonics 10 (2016) 333–339.
[9] H. Song, D. Zhou, X. Bai, et al., Chin. J. Luminescence 44 (2023) 387–412.
[10] Q.S. Chen, J. Wu, X.Y. Ou, et al., Nature 561 (2018) 88–93.
[11] J.H. Heo, D.H. Shin, J.K. Park, D.H. Kim, S.J. Lee, S.H. Im, Adv. Mater. 30 (2018) 1801743.
[12] M. Gandini, I. Villa, M. Beretta, et al., Nat. Nanotechnol. 15 (2020) 462–468.
[13] W. Zhu, W. Ma, Y. Su, et al., Light Sci. Appl. 9 (2020) 112.
[14] X. Sun, M. Xia, Y. Xu, J. Tang, G. Niu, Chin. J. Luminescence 43 (2022) 1014–1026.
[15] A. Kojima, K. Teshima, Y. Shirai, T. Miyasaka, J. Am. Chem. Soc. 131 (2009) 6050–6051.
[16] S.D. Stranks, G.E. Eperon, G. Grancini, et al., Science 342 (2013) 341–344.
[17] G. Li, Z. Su, L. Canil, D. Hughes, et al., Science 379 (2023) 399–403.
[18] X. Yang, J. Han, W. Ruan, et al., Chin. Chem. Lett. 33 (2022) 1425–1429.
[19] S. Lan, B. Pan, Y. Liu, et al., Carbon Energy 5 (2023) e318.
[20] T.C. Jellicoe, J.M. Richter, H.F.J. Glass, et al., J. Am. Chem. Soc. 138 (2016) 2941–2944.
[21] P.P. Sun, Q.S. Li, L.N. Yang, Z.S. Li, Nanoscale 8 (2016) 1503–1512.
[22] L. Liang, P. Gao, Adv. Sci. 5 (2018) 1700331.
[23] Y. Zhang, L. Zhou, L. Zhang, et al., Chin. Chem. Lett. 34 (2023) 107556.
[24] Q. Guo, X. Zhao, B. Song, J. Luo, J. Tang, Adv. Mater. 34 (2022) 2201008.
[25] Y. Jing, Y. Liu, M. Li, Z. Xia, Adv. Opt. Mater. 9 (2021) 2002213.
[26] M.Z. Li, Z.G. Xia, Chem. Soc. Rev. 50 (2021) 2626–2662.
[27] S. Li, J. Luo, J. Liu, J. Tang, J. Phys. Chem. Lett. 10 (2019) 1999–2007.
[28] J. Luo, X. Wang, S. Li, et al., Nature 563 (2018) 541–545.
[29] C.H. Lu, G.V. Biesold, Y.J. Liu, Z.T. Kang, Z.Q. Lin, Chem. Soc. Rev. 49 (2020) 4953–5007.
[30] D.X. Zhu, M.L. Zaffalon, J. Zito, et al., ACS Energy Lett. 6 (2021) 2283–2292.
[31] R.S. Zeng, K. Bai, Q.L. Wei, et al., Nano Res. 14 (2021) 1551–1558.
[32] Z. Tan, J. Li, C. Zhang, et al., Adv. Funct. Mater. 28 (2018) 1801131.
[33] W. Zhang, W. Zheng, L. Li, et al., Angew. Chem. Int. Ed. 61 (2022) e202116085.
[34] J. Sun, W. Zheng, P. Huang, et al., Angew. Chem. Int. Ed. 61 (2022) e202201993.
[35] H. Yang, X. Chen, Y. Chu, et al., Light Sci. Appl. 12 (2023) 75.
[36] S. Li, Q. Hu, J. Luo, et al., Adv. Opt. Mater. 7 (2019) 1901098.
[37] J. Zhao, G. Pan, Y. Zhu, et al., ACS Appl. Mater. Interfaces 14 (2022) 42215–42222.
[38] J.A. McGinnety, Inorg. Chem. 13 (1974) 1057–1061.
[39] B. Su, M. Li, E. Song, Z. Xia, Adv. Funct. Mater. 31 (2021) 2105316.
[40] X.X. Liu, C.D. Peng, L.J. Zhang, D.Y. Guo, Y.X. Pan, J. Mater. Chem. C 10 (2021) 204–209.
[41] X. Cheng, R. Li, W. Zheng, et al., Adv. Opt. Mater. 9 (2021) 2101975.
[42] Y.Y. Jing, Y. Liu, X.X. Jiang, et al., Chem. Mater. 32 (2020) 5327–5334.
[43] Z. Yuan, C. Zhou, Y. Tian, et al., Nat. Commun. 8 (2017) 14051.
[44] K. Han, J. Qiao, S. Zhang, et al., Laser Photonics Rev. 17 (2023) 2200458.
[45] H. Li, M. Zhang, Y. Li, et al., Adv. Opt. Mater. 11 (2023) 2300429.
[46] T. Chang, Q.L. Wei, R.S. Zeng, et al., J. Phys. Chem. Lett. 12 (2021) 1829–1837.
[47] P.T. Ruhoff, Chem. Phys. 186 (1994) 355–374.